Published in final edited form as:
Adv Mater. 2020 June ; 32(22): e2001862. doi:10.1002/adma.202001862.

A Porous Au@Rh Bimetallic Core–Shell Nanostructure as an H_2O_2-Driven Oxygenerator to Alleviate Tumor Hypoxia for Simultaneous Bimodal Imaging and Enhanced Photodynamic Therapy

Jinping Wang,
Department of Biomedical Engineering, Stevens Institute of Technology, Hoboken, NJ 07030, USA

Jingyu Sun,
Department of Chemistry and Chemical Biology, Stevens Institute of Technology, Hoboken, NJ 07030, USA

Wei Hu,
Department of Chemistry and Chemical Biology, Stevens Institute of Technology, Hoboken, NJ 07030, USA

Yuhao Wang,
Department of Biomedical Engineering, Stevens Institute of Technology, Hoboken, NJ 07030, USA

Tsengming Chou,
Laboratory for Multiscale Imaging, Stevens Institute of Technology, Hoboken, NJ 07030, USA

Beilu Zhang,
Department of Chemistry and Chemical Biology, Stevens Institute of Technology, Hoboken, NJ 07030, USA

Qiang Zhang,
Department of Biomaterials, Key Laboratory of Biomedical Engineering of Fujian Province, State Key Lab of Physical Chemistry of Solid Surface, College of Materials, Xiamen University, Xiamen, Fujian 361005, P. R. China

Lei Ren,
Department of Biomaterials, Key Laboratory of Biomedical Engineering of Fujian Province, State Key Lab of Physical Chemistry of Solid Surface, College of Materials, Xiamen University, Xiamen, Fujian 361005, P. R. China

Hongjun Wang

---

hongjun.wang@stevens.edu.

Supporting Information
Supporting Information is available from the Wiley Online Library or from the author.

Conflict of Interest
The authors declare no conflict of interest.

Department of Biomedical Engineering, Stevens Institute of Technology, Hoboken, NJ 07030, USA; Department of Chemistry and Chemical Biology, Stevens Institute of Technology, Hoboken, NJ 07030, USA

Abstract

In treatment of hypoxic tumors, oxygen-dependent photodynamic therapy (PDT) is considerably limited. Herein, a new bimetallic and biphasic Rh-based core–shell nanosystem (Au@Rh-ICG-CM) is developed to address tumor hypoxia while achieving high PDT efficacy. Such porous Au@Rh core–shell nanostructures are expected to exhibit catalase-like activity to efficiently catalyze oxygen generation from endogenous hydrogen peroxide in tumors. Coating Au@Rh nanostructures with tumor cell membrane (CM) enables tumor targeting via homologous binding. As a result of the large pores of Rh shells and the trapping ability of CM, the photosensitizer indocyanine green (ICG) is successfully loaded and retained in the cavity of Au@Rh-CM. Au@Rh-ICG-CM shows good biocompatibility, high tumor accumulation, and superior fluorescence and photoacoustic imaging properties. Both in vitro and in vivo results demonstrate that Au@Rh-ICG-CM is able to effectively convert endogenous hydrogen peroxide into oxygen and then elevate the production of tumor-toxic singlet oxygen to significantly enhance PDT. As noted, the mild photothermal effect of Au@Rh-ICG-CM also improves PDT efficacy. By integrating the superiorities of hypoxia regulation function, tumor accumulation capacity, bimodal imaging, and moderate photothermal effect into a single nanosystem, Au@Rh-ICG-CM can readily serve as a promising nanoplatform for enhanced cancer PDT.

Keywords

bimetallic Rh-based core–shell nanostructures; bimodal imaging; endogenous oxygenation; enhanced photodynamic therapy; hypoxia alleviation

Hypoxia is a hallmark of solid tumors. With burgeoning tumor growth, intratumoral O_2 supply as a result of poor blood flow from the aberrant vasculature can hardly meet the ever-increasing metabolic demands of tumors and inevitably leads to notable hypoxia in the local tumor environment (typically, $pO_2 \leq 2.5$ mmHg).[1] Under such hypoxic circumstances, oxygen-dependent therapies such as radiotherapy, chemotherapy, and photodynamic therapy (PDT) face significant or complete loss of therapeutic efficacy.[2]

This is of particular importance to PDT, which depends on the ability of photosensitizers to transfer energy from light to tumor-dissolved oxygen (O_2) for generating cytotoxic reactive oxygen species (ROS), such as singlet oxygen ($^1O_2$), to kill tumor cells.[3] As an oxygen-dependent treatment modality, the efficiency of PDT is normally compromised due to the intrinsic hypoxia of tumors,[4] and exacerbated along with further consumption of O_2 by PDT.[5] In addition to the need for improving laser penetration depth,[6] it is also essential to address hypoxia-induced resistance with current PDT for deep tumor therapy.[7]

Various nanomaterial-enabled systems have been explored to alleviate tumor hypoxia.[8] So far, three major strategies have been taken, including: 1) the use of oxygen-carrying nanomaterials, based on perfluorocarbon or hemoglobin, for direct delivery of oxygen into tumor sites,[9] 2) in situ generation of oxygen upon decomposition of chemicals (such as C_3N_4 and CaO_2) carried by nanomaterials to the tumor site,[10] and 3) in situ conversion of endogenous hydrogen peroxide (H_2O_2) into oxygen using catalytic nanoparticles.[11] As a result of abnormal pathophysiologic processes in tumors (e.g., overexpression of NADPH oxidase (NOX) enzymes), elevated H_2O_2 at a typical generation rate of 5 nmol per 10^5 cells h^{-1} is consistently observed in the tumor microenvironment.[12] Thus, the strategy to generate oxygen out of elevated endogenous H_2O_2 will exhibit a good tumor therapeutic efficiency.[13] In this regard, development of nanomaterials that can catalyze endogenous H_2O_2-to-O_2 conversion has received growing interest.[14] Recent efforts have been made to fabricate “nanoenzymes” mainly from catalase or manganese (Mn)-based materials, such as catalase-containing poly(lactic-*co*-glycolic acid) nanocapsules,[15] MnO_2 nanoparticles,[16] and $MnFe_2O_4$ nanoparticles,[17] for O_2-dependent tumor therapy. Despite their efficient decomposition of H_2O_2 into O_2, foreseeable challenges with such nanomaterials, such as the thermo-instability and protease-sensitivity of catalase (limited processing conditions and shelf life) and pH-dependent catalysis of Mn-based materials (only suitable for acidic tumor environments), motivate continuous endeavors to develop more robust enzyme-like systems. Preferably, some new nanosystems that have good thermostability while retaining catalaselike activity independent of pH can be achieved to effectively resolve the hypoxia-driven resistance to tumor therapy.

Very recently, rhodium (Rh)-based nanostructures have been explored for possible biological applications as near-infrared (NIR)-absorbing nanomaterials in tumor photothermal therapy (PTT).[18] More importantly, Rh showed intrinsic catalase-like activity to decompose H_2O_2 into O_2,[19] and Rh alloys exhibited better catalytic effect.[20] Built on the established evidence, we therefore hypothesized that Rh-based bimetallic nanomaterials could effectively and continuously catalyze O_2 production from endogenous H_2O_2 in the tumor site independent of pH, and consequently ameliorate local hypoxia to enhance PDT. Furthermore, the NIR photothermal conversion capacity of Rh-based nanomaterials may see additional benefits in PDT. Previous reports highlighted that the mild photothermal effect from NIR-absorbing nanoagents could enhance cellular uptake of loaded photosensitizers[21] and increase intratumoral blood flow to facilitate oxygenation of tumors to reduce hypoxia-associated resistance.[22] To this end, the use of Rh-based bimetallic nanomaterials as a delivery system for PDT photosensitizers could also improve the therapeutic outcomes of PDT.

In this work, we synthesized porous Au@Rh core–shell nanostructures as the basic platform and then further formulated a nanotherapeutic reagent, i.e., Au@Rh-ICG-CM nanocomposites, by loading the photosensitizer indocyanine green (ICG) in the pores and coating with cancer cell membrane (CM) (Scheme 1). Adoption of the bimetallic core–shell nanocrystal design with a porous shell would allow for the exposure of reactants to two metals while modulating the unique core/shell boundary interactions for optimal catalysis via electronic and surface strain effects.[23] Furthermore, the porous shell with increased surface area could effectively trap the therapeutics.[24] The physicochemical and biological properties of Au@Rh-ICG-CM were studied in vitro and in vivo to comprehensively evaluate the photothermal conversion performance, H_2O_2-to-O_2 decomposition, efficient $^1O_2$ generation capacity, cellular uptake, tissue distribution, tumor therapeutic effects, and biosafety. The prepared Au@Rh-ICG-CM nanosystem displays multifaceted unique features, including: 1) Au@Rh-CM can decompose endogenous H_2O_2 to rapidly generate O_2 in a neutral or acidic environment; 2) Porous cavities of Au@Rh-CM in combination with the trapping ability of CM can increase the loading efficiency of ICG while stabilizing its activity during biological transport without early release; 3) Broadband photoabsorption of Au@Rh-CM like a blackbody[25] enables the excitation of loaded photosensitizers with high tissue penetration NIR laser for concurrent PTT and PDT; 4) The mild photothermal effect of Au@Rh-ICG-CM under 808-nm laser irradiation favors its catalytic decomposition of H_2O_2 and facilitates cellular uptake of ICG; 5) Due to homologous binding capability of cancer CM, selective tumor accumulation of Au@Rh-CM leads to effective delivery of photosensitizer to tumor site for improved PDT specificity; 6) The in vivo fluorescence and photoacoustic (PA) imaging capabilities from respective loaded ICG and Au@Rh afford a means to trace tissue distribution of Au@Rh-ICG-CM as well as guide the therapeutic process. Along with successful demonstration of such Au@Rh bimetallic nanoparticles as a multifunctional oxygenator to treat hypoxic tumors, this study also provides blueprints to design other bimetallic nanoplatforms with varying attributes for tumor theranostics.

Due to its relatively high surface energy (124, 144, and 147 meV $Å^{-2}$ for the [111], [100], and [110] facets, respectively), synthesis of Rh nanostructures from Rh precursor salts via chemical reduction normally requires elevated reaction temperature and prolonged reaction time, in contrast to the mild and rapid reactions for other noble metal (e.g., Pt, Pd, and Au) nanostructures.[26] Taking advantage of such differences in reduction, we accordingly designed an effective yet simple route to synthesize bimetallic nanostructures of Au@Rh with solid Au as the core and mesoporous Rh as the shell at a relatively lower temperature (60 °C) than other approaches (e.g., 190 °C).[27] With the presence of mesopores through the Rh shell, free access of H_2O_2 and large catalysis surface area are expected to result in a maximal O_2 conversion efficiency. To generate controllable mesopores in the Rh shell, a modified micelle-templating method[28] was adopted. As shown in Figure 1a, micelles of a block copolymer poly(ethylene oxide)-*b*-poly(methyl methacrylate) (PEO_{10500}-*b*-$PMMA_{18000}$) were first created by dissolving in a N,N-dimethylformamide (DMF) and water (3:2) mixture and then Au and Rh precursors (12×10^{-3} M $HAuCl_4$ and 40×10^{-3} M Na_3RhCl_6) were added, respectively. In the solution, Na_3RhCl_6 crystals are dissolved into Na^+ and $[Rh(H_2O)_{3-x}Cl_{6-x}]^{(3-x)-}$ ion complexes.[28a] Through hydrogen bonding, $[Rh(H_2O)_{3-x}Cl_{6-x}]^{(3-x)-}$ were brought to the PEO surface of micelles to form PEO-*b*-PMMA micelle/Rh nanocomposites. Meanwhile, free $AuCl_4^-$ in the solution was rapidly reduced to Au^0 by ascorbic acid (AA) to form solid nanoparticles (see the time-section result of 0.5 h reaction, Figure S1a, Supporting Information). By sharing the electron cloud between Au^0 and $[Rh(H_2O)_{3-x}Cl_{6-x}]^{(3-x)-}$, PEO-*b*-PMMA micelle/Rh nanocomposites were attracted to the surface of Au nanoparticles and gradually assembled into multilayered shells (Figure S1a, Supporting Information). The progress of Au@Rh reduction can also be visually monitored via the color change of the reaction solution (Figure S1b, Supporting Information). Modulating the ratio between $HAuCl_4$ and Na_3RhCl_6 enabled the respective control of the Au core size and the Rh shell thickness (Figure S2a,b, Supporting Information). At the ratio of 1:3.3 (12×10^{-3} M $HAuCl_4$ and 40×10^{-3} M Na_3RhCl_6), a typical shell thickness of 30.8 ± 2.5 nm and core size of 32.6 ± 3.9 nm were achieved

(Figure S2c, Supporting Information). Upon completion of the reduction of Na_3RhCl_6 into Rh, PEO-*b*-PMMA micelles were then removed through consecutive washing/centrifugation cycles to yield porous Au@Rh core–shell nanostructures (Figure S3, Supporting Information). To confirm the formation of desired nanostructures, both scanning electron microscopy (SEM) and transmission electron microscopy (TEM) characterization were performed. SEM examination of the overall morphology of as-prepared Au@Rh nanostructures revealed their monodispersity with rather uniform size and shape (Figure 1b). The mean diameter of Au@Rh nanoparticles is 95.6 ± 3.6 nm (Figure S4, Supporting Information), which allows for prolonged circulation in the blood and enhanced extravasation into tumors.[29] Close examination of Au@Rh nanostructures with SEM showed well-defined mesopores throughout the outer surface (Figure 1b inset). Further TEM visualization of Au@Rh nanostructures revealed the consistent presence of a dense core surrounded by porous shell with a clear boundary in between (Figure 1c). It is noted that the shell thickness among the nanostructures is rather uniform (30.8 ± 2.5 nm) and homogeneous pores were seen across the entire thickness. As evidenced in nitrogen adsorption isotherms, such mesoporous structures provided as high as 0.99 $cm^3\ g^{-1}$ of pore volume (Figure S5a, Supporting Information), superior over other Rh nanomaterials such as nanosheets[18] in terms of sufficient cavity for drug molecule loading. Meanwhile, the average mesopore size is 9.4 nm (Figure S5b, Supporting Information), larger than most common mesoporous nanostructures,[30] implying easy accessibility of the interior pores to large biomolecules. The structural stability of porous Au@Rh was also tested upon a prolonged storage (7 and 30 d). No changes of the morphology and mesoporous structures were noticed based on the SEM examination even after 30 d (Figure S6, Supporting Information). To confirm the mesostructural periodicity (i.e., pore-to-pore distance), the low-angle X-ray diffraction (XRD) measurement was performed. A single peak located at 0.45° was observed in the low XRD pattern, indicating the closely packing of uniformly sized pores (Figure S5c, Supporting Information). Based on the peak mean value, the pore-to-pore distance was calculated to be ≈20 nm. As shown in Figure S7 (Supporting Information), the pore size was ≈10 nm, consistent with the Brunauer–Emmett–Teller (BET) result (9.4 nm). In addition, 3D electron tomography of Au@Rh reconstructed from a tilted series of microscopy images (Video S1, Supporting Information) also confirmed that the distribution of interconnected mesopores throughout the shell on the surface of Au core to form a bicontinuous structure. In the wide-angle XRD pattern of the Au@Rh, five characteristic diffraction peaks of Au and Rh (111), (200), (220), (311), and (222) were, respectively, observed (Figure S5d, Supporting Information), which agreed with the results of selected area electron diffraction (SAED) patterns (Figure S8c, Supporting Information). These peaks and concentric rings of spots suggest the random aggregation of crystal grains in the Au@Rh nanostructures, rather than the oriented growth. Based on the Rh (111) diffraction peak, the crystalline grain size was calculated using the Scherrer equation to be around 5.3 nm, which also matched the grain size of about 4.5 nm within the mesoporous shell as measured in TEM images (Figure S8a,b, Supporting Information). Energy-dispersive X-ray spectroscopy (EDS) elemental mapping further confirmed that the core was made of Au and the porous shell was made of Rh (Figure 1f and Figure S9, Supporting Information). With readily tunable size of Au core and shell thickness, such bimetallic nanostructures can achieve various properties for versatile applications such as the thermoresponsive drug release systems.

To retain biomolecules within the mesopores along with improved targeting to cancer cells, we explored the possibility of coating Au@Rh nanostructures with cancer CM. CM was easily obtained by lysing cancer cells (i.e., MDA-MB-231 breast cancer cells) with the hypotonic lysis buffer[31] and then collecting the fragmented cell membrane in the supernatant. To assure a full coverage of the particle surface, excessive CM (typically from 10^7 cells) was used for 0.5 mg Au@Rh nanostructures. As a result of the mechanical force provided by ultrasonic energy, fragmented CM was able to reassemble on the surface of nanostructures to establish a continuous membrane.[32] CM coating had negligible effect on the overall morphology of Au@Rh nanostructures (Figure 1d), while zoomed-in examination indeed showing the presence of a layer of CM on the nanostructure surface (Figure 1d inset vs Figure 1c inset). After CM coating, the mean size of nanostructures increased to 104.9 ± 2.8 nm (Figure S10, Supporting Information), indicating that the thickness of CM layer was about 5 nm. Surface zeta potential of Au@Rh nanostructures before and after CM coating (Figure S11a, Supporting Information) was measured to further confirm the attachment of CM. After CM coating, the surface zeta potential of Au@Rh-CM nanostructures changed from −6.2 to −21.3 mV, which was close to the zeta potential of MDA-MB-231 CM (−24.5 mV). Fourier transform infrared (FTIR) spectra showed the presence of signature absorptions of amide bond, phosphate, and carbohydrate region of CM in the Au@Rh-CM nanostructures thereby confirming the successful attachment of CM (Figure S11b, Supporting Information). Protein analysis using sodium dodecyl sulfate-polyacrylamide gel electrophoresis (SDS-PAGE) also demonstrated that the presence and maintenance of protein contents of purified CM in Au@Rh-CM in contrast to the minimal protein content from the Au@Rh (Figure 1e). Following successful coating of CM onto Au@Rh nanostructure, it becomes essential to understand the stability of such structures especially for future in vitro and in vivo use. Stability tests of Au@Rh-CM nanostructures were, respectively, carried out in deionized (DI) water, phosphate-buffered saline (PBS, pH = 7.4), and cell culture media with 10% serum. Upon incubation for 30 d in individual solutions, the Au@Rh-CM nanostructures remained well suspended without noticeable aggregation or precipitation (Figure S12, Supporting Information) or any noted size changes (Table S1, Supporting Information) for the entire investigating period. In contrast, precipitation was readily seen with Au@Rh only particles (Figure S12a, Supporting Information). Apparently, the demonstrated stability of Au@Rh-CM was mainly attributed to the stealth effect of negatively charged CM.[33]

As Au@Rh nanostructures are primarily responsible for the photoabsorption behavior of Au@Rh-CM nanostructures, we therefore only established the UV–vis–NIR spectra of Au@Rh nanostructures. Interestingly, the synthesized Au@Rh nanostructures exhibited strong broadband absorption (Figure 1g), similar to a blackbody.[25] With this said, Au@Rh nanostructures could effectively convert the absorbed photonic energy from a broad spectrum of wavelengths including NIR into heat. Thus, it becomes feasible to load NIR-activated photosensitizers in Au@Rh-CM to achieve concurrent PTT and PDT upon single NIR laser irradiation, which can simplify treatment procedures and reduce therapy time. To demonstrate this, the photosensitizer ICG was particularly chosen for its excitability with a deep tissue penetration 808-nm NIR laser approved for clinical use by the U.S. Food and Drug Administration (FDA),[34] and ICG was loaded into the mesopores of Au@Rh-CM nanostructures. As shown in Figure 1g, Au@Rh-ICG-CM nanocomposites did exhibit a slight redshift of characteristic ICG absorption peak from 780 to 810 nm in contrast to no noticeable shift of the physically mixed Au@Rh-CM and free ICG, confirming successful loading of ICG in Au@Rh-CM nanostructures. During incubation with ICG solution, the large mesopores and high surface area of the porous Rh shells in Au@Rh nanostructures could effectively trap ICGs and therefore result in a high payload. Indeed, a high loading efficiency of 15.6 ± 2.1 wt% was achieved, which was much higher than that of previously reported nanostructures.[35] Parallel studies were also performed to determine the photothermal capabilities of Au@Rh-CM and Au@Rh-ICG-CM. Respective aqueous solution of Au@Rh-CM (0.1 mg mL^{-1} in DI water) and Au@Rh-ICG-CM (0.1 mg mL^{-1} in DI water) was irradiated with an 808-nm laser at a power density of 0.3 W cm^{-2}. The time-dependent temperature changes were recorded using a digital thermocouple thermometer. As shown in Figure 1h, after 6 min irradiation the temperature of both Au@Rh-CM and Au@Rh-ICG-CM solutions increased dramatically, significantly higher than that of free ICG or DI water. Although ICG could also act as PTT agent, the combination of the relatively low concentration of free ICG (18.5 µg mL^{-1}) and low 808-nm laser power (0.3 W cm^{-2}) only resulted in a weak PTT effect. Photothermal images of Au@Rh-CM and Au@Rh-ICG-CM solutions confirmed heat generation within the solution (Figure 1i). Clearly, the dramatic temperature elevation is ascribed to the high photothermal efficiency of Au@Rh nanostructures. Compared to Au@Rh-CM, the temperature of Au@Rh-ICG-CM solution was slightly higher, reaching as high as 44.3 °C. Such a difference is mainly from ICG loaded in the nanostructures in consideration of its maximum absorption peak at 800-nm wavelength and noted temperature increase after 808-nm laser irradiation. Interestingly, the observed photothermal effect of Au@Rh-CM is relatively mild compared to other nanostructures such as Au nanoshells, resulting in a high temperature increase (e.g., 70 °C).[36] As reported, mild-to-moderate hyperthermia is favorable for cancer treatment by regulating tumor vascular perfusion, lymphocyte trafficking, inflammatory cytokine expression, tumor metabolism, and innate and adaptive immune function.[37] As such, Au@Rh-ICG-CM is expected to improve subsequent PDT efficacy as an adjuvant nanosystem.

Based on the evidence that platinum group metals exhibited the catalytic activity of decomposing H_2O_2,[19] we therefore hypothesized that Au@Rh-CM bimetal nanostructures with porous Rh shell can effectively catalyze the decomposition of H_2O_2 into O_2. Bubble formation of released O_2 in a reaction solution could be used as an indicator as the onset of catalyzed decomposition. To better manifest this, a high concentration of H_2O_2 (20×10^{-3} M) was used. As shown in Figure S13 (Supporting Information), formation of abundant O_2 bubbles was observed upon addition of H_2O_2 (20×10^{-3} M) in the tubes containing Au@Rh-CM (50 µg/mL). No bubbles were observed in tubes with either H_2O_2 (20×10^{-3} M) or Au@Rh-CM (50 µg mL^{-1}) alone. Such an observation verifies that Au@Rh-CM indeed has catalase-like catalysis capability.

Previous findings highlighted the superior catalytic capabilities of bimetallic structures to their monometallic counterparts.[38] To elaborate the advantages of bimetallic Au@Rh, porous Rh nanoparticles with comparable sizes were also synthesized and used to evaluate their catalytic efficiency. In recognition of the high catalytic capacity of platinum (Pt)-based nanomaterials in decomposing endogenous H_2O_2 to improve tumor hypoxia,[14d,39] porous core–shell Au@Pt nanostructures were also similarly prepared and used as a benchmark to determine the catalytic efficiency of Au@Rh nanostructures. As confirmed by SEM, the prepared Rh nanoparticles and Au@Pt nanostructures both showed similar size and porous morphology to Au@Rh (Figure 1j inset). Steady-state kinetics of Au@Rh, Rh, and Au@Pt toward H_2O_2 decomposition was established by measuring the initial decomposition rates as a function of H_2O_2 concentration using the Goth method.[40] As reported, the catalytic process typically follows a Michaelis–Menten reaction model.[40b] Based on the corresponding Lineweaver–Burk plots (Figure 1j,k), key enzyme kinetic parameters including Michaelis–Menten constants (K_m), catalytic constants (K_{cat}), and maximum reaction velocity (V_{max}) were calculated (Figure 1l). In the catalytic reactions, K_m represents the enzyme affinity for substrate (low K_m indicates a high affinity), while K_{cat} represents the enzyme activity (high K_{cat} implies a high catalytic ability).[41] Our results showed that the V_{max} value for Au@Rh nanostructures was almost 14 times that of porous Rh nanoparticles, confirming the much higher catalytic activity of bimetallic Au@Rh nanostructures than that of monometallic Rh nanomaterials. In the comparison between Au@Pt and Au@Rh, we noticed that the K_m value of Au@Rh nanostructures was a little lower than that of Au@Pt, however, its K_{cat} value was much higher than that of Au@Pt, implying significantly improved catalytic capability with Au@Rh nanostructures. Obviously, porous core–shell Au@Rh nanostructures exhibited a strong affinity for H_2O_2 and high catalase-like activity.

Further studies were done to evaluate the catalysis capacity of Au@Rh-CM under a pathophysiologically relevant concentration (1×10^{-4} M).[42] To better understand the O_2 generation kinetics of Au@Rh-CM-enabled H_2O_2 decomposition, an O_2 probe of $[Ru(dpp)_3]Cl_2$ (RDPP), whose fluorescence can be immediately quenched by O_2,[43] was used to monitor O_2 generation. As shown in Figure 2a, addition of H_2O_2 (1×10^{-4} M) to the Au@Rh-CM/RDPP aqueous solution caused immediate decrease of fluorescence intensity of RDPP for the first 10 min. Afterward, the fluorescence intensity loss remained at a similar level for the next 20 min, indicating the approach to an equilibrium of H_2O_2 to O_2 conversion with an ≈77.4 ± 2.8% conversion rate. In contrast, no obvious loss of fluorescence intensity was found with H_2O, H_2O_2, or Au@Rh-CM without H_2O_2, further confirming that O_2 generation was from H_2O_2 and the participation of Au@Rh-CM was required. In addition, the O_2 generation capacity of Au@Rh-CM under different pH conditions was also examined (Figure S14a, Supporting Information). Here, pH 5 was used to mimic the real acidic tumor microenvironment.[44] As shown in Figure S14a (Supporting Information), comparable O_2 generation capacity was seen between pH 7.4 and 5.0, suggesting the applicability of Au@Rh-CM to physiological pH. It is worth mentioning that the elevated temperature as a result of mild/moderate photothermal effect of Au@Rh-CM (Figure 1h) might facilitate the catalytic decomposition of H_2O_2 to O_2. To demonstrate this assumption, the Au@Rh-CM-enabled H_2O_2 decomposition was also evaluated at an elevated temperature (i.e., 42°C). Compared to room temperature (25 °C), elevated temperature (42 °C) indeed accelerated the rate of H_2O_2 decomposition and improved the conversation efficiency to 93.9 ± 3.4% (Figure S14b, Supporting Information). Furthermore, time-dependent change of H_2O_2 concentration in the Au@Rh-CM-enabled catalytic reaction was also monitored by measuring the absorbance of H_2O_2 at 240 nm (Figure S15, Supporting Information). As shown in Figure 2b, continuous decrease of H_2O_2 concentration in the reaction was observed, however a sharp decrease was only seen for the first 10 min, which agreed well with the trend of O_2 generation. Such a close correlation between H_2O_2 consumption and O_2 generation could ameliorate local hypoxia conditions of tumor.

During PDT treatment, generation of toxic $^1O_2$ is essential to eradicate tumor cells. Hence, $^1O_2$ production with the presence of Au@Rh-ICG-CM was first investigated in an acellular setting, i.e., solution-based study, using 1,3-diphenylisobenzofuran (DPBF) as a probe, which could be oxidized by ROS irreversibly and resulted in the decrease of its characteristic absorption peak at 410 nm. As seen in Figure 2c, the combination of Au@Rh-CM and laser irradiation (808 nm, 0.3 W cm^{-2}) caused negligible changes of the absorption intensity of DPBF at 410 nm, while a rapid decrease occurred with a combination of Au@Rh-ICG-CM and laser irradiation. Such results demonstrated that Au@Rh-CM itself had minimum contribution to direct ROS formation and ICG loaded in the Au@Rh-CM was primarily responsible for ROS production. Such results demonstrated that Au@Rh-CM itself had minimum contribution to direct ROS formation and ICG loaded in the Au@Rh-CM was primarily responsible for ROS production. In addition, time-dependent UV–vis–NIR absorption spectra were obtained with solutions containing Au@Rh- ICG-CM under laser irradiation. The measurement showed that $^1O_2$ production (i.e., peak at 410 nm) was time-dependent and a majority was formed within 10 min as demonstrated by significantly reduced absorption after 10 min (Figure S16, Supporting Information). Considering that DPBF can react with all ROS including H_2O_2 (Figure 2c),[45] singlet oxygen sensor green (SOSG) with good selectivity toward $^1O_2$ than other species (e.g., hydrogen peroxide or hydroxyl radicals),[46] was used to evaluate the $^1O_2$ production. Along with the consumption of soluble O_2 in the solution, decelerated production of $^1O_2$ was expected with Au@Rh-ICG-CM (Figure 2d). In this regard, addition of exogenous H_2O_2 (1×10^{-4} M) into the system could boost O_2 level via Au@Rh-CM-enabled H_2O_2 decomposition and consequently increase further $^1O_2$ production (Figure 2d). Indeed, the combination of H_2O_2 and Au@Rh-ICG-CM yielded the highest $^1O_2$ level. Following the acellular solution-based studies, intracellular $^1O_2$ generation by Au@Rh-ICG-CM was also investigated in breast cancer cells (MDA-MB-231) using SOSG as the probe, which reacts with $^1O_2$ to generate a green fluorescence endoperoxide product.[7a] Under 808-nm laser irradiation, strong intracellular green fluorescence was detected in cells incubated with either free ICG or Au@Rh-ICG-CM, with no detectable green fluorescence in untreated cells (Figure 2e). The comparable intracellular SOSG fluorescence intensity (Figure S17a, Supporting Information) between Au@Rh-ICG-CM and free ICG groups suggests that both free ICG and Au@Rh-ICG-CM similarly produce $^1O_2$ under 808-nm laser irradiation. As such, cellular uptake of Au@Rh-ICG-CM should take place prior to the intracellular release of its ICG cargo. Thus, internalization and intracellular localization of Au@Rh-ICG-CM in MDA-MB-231 cells were investigated with both fluorescence microscopy and TEM. After 6 h incubation with Au@Rh-ICG-CM, MDA-MB-231 cells showed strong red fluorescence, similar to those with free ICG (Figure 2f and Figure S17b, Supporting Information), indicating successful internalization of Au@Rh-ICG-CM. Meanwhile, it was found that core–shell Au@Rh-ICG-CM nanostructures were mainly located in the cytoplasm and lysosome (Figure 2g). Efficient cellular uptake of Au@Rh-ICG-CM by MDA-MB-231 cells may come from the homologous CM coating,[47] ensuring O_2 and subsequent toxic $^1O_2$ generation for PDT (Figure 3a). To further illustrate the homologous targeting effect of Au@Rh-ICG-CM, a coculture of GFP-labeled human umbilical vein endothelial cells (HUVECs) and nonlabeled MDA-MB-231 cells was treated with respective Au@Rh-ICG-CM or ICG only. As shown in Figure 2h and Figure S18 (Supporting Information), stronger ICG fluorescence (red) was found in MDA-MB-231 cells than that in HUVECs with Au@Rh-ICG-CM treatment while comparable red fluorescence intensity in HUVECs and MDA-MB-231 cells was seen with free ICG treatment, consistent with the flow cytometry analysis results (Figure 2i). Cellular uptake of Au@Rh-ICG-CM under a mild photothermal effect was also evaluated. Since both 808 nm and 1064 nm laser irradiation of Au@Rh-CM led to identical temperature increases (Figure S19, Supporting Information), 1064 nm laser was particularly used to induce a mild photothermal effect in order to avoid fluorescence loss of ICG under 808 nm laser irradiation. Interestingly, after 1064-nm laser irradiation for 3 min, elevated red fluorescence (ICG) intensity was observed in MDA-MB-231 cells compared to that without laser irradiation (Figure S20, Supporting Information), suggesting a favorable influence of mild photothermal effect on cellular uptake of Au@Rh-ICG-CM as well as the release of ICG from Au@Rh-CM (Figure S21, Supporting Information).

Cellular uptake of Au@Rh-CM should be able to help alleviate hypoxia (purposely induced via the N_2 atmosphere) by generating intracellular O_2. To better mimic the tumor microenvironment with endogenous H_2O_2, 1×10^{-4} M H_2O_2 was supplemented to the culture.[14a] Using RDPP as an indicator for intracellular O_2 level (red fluorescence is quenched by O_2),[12a] we found that MDA-MB-231 cells treated with Au@Rh-CM and H_2O_2 displayed the lowest fluorescence compared to other groups (no treatment, H_2O_2 alone, Au@Rh-CM alone) in N_2 atmosphere (Figure 3b). Semiquantification of the fluorescence intensity using ImageJ revealed that no treatment group was ≈9.5 times that of Au@Rh-CM+ H_2O_2 group, demonstrating the catalytic capability of cellular Au@Rh-CM in O_2 generation from H_2O_2 (Figure S22a, Supporting Information). The subsequent responsibility of such elevated O_2 for intracellular $^1O_2$ increase by Au@Rh-ICG-CM in N_2 atmosphere was also investigated by using SOSG as the probe. In comparison to negligible fluorescence in other groups (no treatment, Au@Rh-ICG-CM, or Au@Rh-CM plus laser), Au@Rh-ICG-CM and 808-nm laser irradiation (0.3 W cm^{-2}, 3 min) yielded some green fluorescence, but still relatively weak (Figure 3c4 vs c1–3). However, upon addition of H_2O_2 much stronger green fluorescence (Figure 3c5 vs c4) was observed, ≈5.8 times of the no treatment controls (Figure S22b, Supporting Information), suggesting that O_2 generation could increase $^1O_2$ level even under the hypoxic condition.

The cytocompatibility of Au@Rh-ICG-CM and the in vitro cell killing efficacy to MDA-MB-231 via combined PDT and mild PTT were investigated using 3-(4,5-dimethylthiazol-2-yl)-2,5-diphenyltetrazolium bromide (MTT) assay. Both Au@Rh-CM and Au@Rh-ICG-CM themselves showed superior cytocompatibility for all the investigated concentrations (up to 200 µg mL^{-1}) (Figure S23, Supporting Information). However, when combined with laser irradiation (808 nm, 0.3 W cm^{-2}, 3 min), ≈36% cancer cell killing efficiency was achieved with Au@Rh-CM comparably under normoxia (air) or hypoxia (N_2) (Figure S24, Supporting Information) and such killing was mainly ascribed to the mild PTT induced by Au@Rh-CM. Next, the cell killing efficiency under normoxia and hypoxia with or without exogenous H_2O_2 was also evaluated (Figure 3d). Different from Au@Rh-CM, Au@Rh-ICG-CM displayed drastic distinction between normoxia and hypoxia in cell killing capacity, i.e., 84% (air) versus 36% (N_2) with the hypoxic killing similar to that of Au@Rh-CM. As noted, addition of H_2O_2 into the hypoxic culture could boost the killing efficiency to 80%, effectively resolving the challenge of hypoxia-compromised PDT. As observed, the mild cell killing from PTT was dependent on the concentration of Au@Rh-CM or Au@Rh-ICG-CM but independent of O_2 (Figure 3f). However, the dominant cell killing by ICG-enabled PDT was not only dependent on the concentration of Au@Rh-ICG-CM, but also closely related to the presence of O_2 (Figure 3e,f). The hypoxic MTT results were also echoed by live and dead staining of the cells upon various treatments (Figure 3g). Once again, under 808-nm laser irradiation addition of exogenous H_2O_2 to the hypoxic culture with Au@Rh-ICG-CM led to all dead cells in contrast to partial and identical cell death with either Au@Rh-CM or Au@Rh-ICG-CM. The above results confirmed the dependence of $^1O_2$ generation on O_2 during ICG-enabled PDT. More importantly, exogenous addition of H_2O_2 to the culture with Au@Rh-ICG-CM successfully overcame the hypoxia-induced reduction of cell killing, demonstrating that Au@Rh-ICG-CM could effectively catalyze the decomposition of H_2O_2 into O_2 so an adjacent photosensitizer (ICG) could produce $^1O_2$ to eradicate hypoxic tumor cells.

Based on the demonstrated in vitro H_2O_2 decomposition capability (Figure 3b), in vivo utility of Au@Rh-ICG-CM for cancer therapy was evaluated on MDA-MB-231-tumor-bearing mice. Loading of fluorescent ICG in Au@Rh-CM allowed the nanosystems use for in vivo imaging with NIR fluorescence. Thus, fluorescence images of mice were obtained before and after i.v. injection of Au@Rh-ICG-CM and free ICG was used for control. During the entire observation period, free ICG showed minimal fluorescence signal in tumor tissues and by 24 h postinjection relatively weak fluorescence signal was detected within the whole body (Figure 4a), indicating that free ICG had no preference to accumulate in tumor and was quickly excreted from the body. In contrast, Au@Rh-ICG-CM gradually accumulated in the tumor sites most likely as a result of homologous binding of CM to MDA-MB-231 cells and the strongest fluorescence signal was seen at 12 h postinjection of Au@Rh-ICG-CM, suggesting a lapse of 12 h is necessary prior to in vivo PDT. To better characterize the biodistribution of ICG between free and loaded formats, major organs (heart, liver, spleen, lung, and kidneys) and tumors were collected after 24 h for ex vivo fluorescence imaging. As evidenced, strong fluorescence signal still presented in the tumor tissue with Au@Rh-ICG-CM injection along with expected liver accumulation, and such findings were further confirmed by semi-quantification of the fluorescence intensity in various tissues (Figure 4b,c). Clearly, the fluorescence imaging capability is beneficial to real-time monitor the real-time in vivo distribution of Au@Rh-ICG-CM and provides guidance for specific tumor PDT.

Given the strong NIR absorption of Au@Rh-ICG-CM, we also anticipated that this nanosystem could serve as a contrast agent for PA imaging.[48] To demonstrate this capability, Au@Rh-ICG-CM solutions at different concentrations were performed for PA imaging and intense photoacoustic signals were detected from Au@Rh-ICG-CM in a linear response to its concentration (Figure 4d). Then efforts were extended to in vivo PA imaging to verify the high tumor accumulation of Au@Rh-ICG-CM (Figure 4e). Compared to negligible PA signal prior to i.v. injection of Au@Rh-ICG-CM (i.e., baseline), continuous increase of PA signal in the tumor region was seen soon after i.v. injection of Au@Rh-ICG-CM and reached the maximum at 12 h (i.e., ≈7 times the baseline) (Figure 4e,f), which coincided with the fluorescence imaging results (Figure 4a). Both fluorescence and PA imaging results have highlighted the superiority of Au@Rh-ICG-CM in terms of allowing for precisely tracking their tumor accumulation via self-enabled fluo-rescence/PA bimodal imaging capacities.

Recognizing the high accumulation of Au@Rh-ICG-CM in tumor tissues, efforts were made to utilize such nanocomposites for in vivo tumor therapy. MDA-MB-231-tumor-bearing Balb/c nude mice randomly divided into five groups and were, respectively, treated with PBS, laser irradiation only, Au@Rh- ICG-CM only, Au@Rh-CM with laser irradiation, and Au@Rh- ICG-CM with laser irradiation. To assure maximum accumulation of Au@Rh-ICG-CM in the tumor region, the mice were not exposed to 808-nm laser (0.3 W cm^{-2}) until 12 h after Au@Rh-ICG-CM injection. Considering the mild photothermal effect of Au@Rh-ICG-CM (Figure 1h), exposure of the tumor region accumulated with Au@Rh-ICG-CM to laser could increase the local temperature. Indeed, 5 min irradiation resulted in a temperature increase to about 43.0 from 35.5 °C as recorded by infrared camera (Figure 5a). Such a mild temperature increase is beneficial, not only inducing PTT of cancer via hyperthermal destruction but also promoting tumor uptake of nanopar- ticles.[49] With established evidence, i.e., Au@Rh-ICG-CM was able to facilitate H_2O_2 decomposition and subsequently promote $^1O_2$ generation; improved PDT of tumor was also expected. As shown in Figure 5b, significant inhibition and size reduction was seen with tumors treated with Au@Rh-ICG-CM plus laser irradiation for all the investigated time points. Notable size reduction of tumors happened as soon as 2 d after treatment and by 16 d the tumors became very tiny and even invisible in some cases (Figure 5b and Figure S25, Supporting Information). Tumors treated with Au@Rh-CM plus laser irradiation exhibited suppressed growth only for the first 6 d and then slowly regained growth potential though still much lower than those treated with PBS, laser alone, or Au@Rh-ICG-CM alone (Figure 5b). Actually, neither laser alone nor Au@Rh-ICG-CM alone exhibited noticeable inhibition to tumor growth (Figure 5b and Figure S25, Supporting Information). The endpoint weighing of harvested tumors from each treatment group further affirmed the size measurement results (Figure 5c). The observed in vivo tumor inhibition effects from various treatments agreed well with in vitro MDA-MB-231 cell results (Figure S24, Supporting Information). The collected tumors were also processed for intratumor histologic assessment by staining thin cross sections with hematoxylin and eosin (H&E). Based on cell morphology, various treatments induced distinctive therapeutic outcomes. The combination of Au@Rh-ICG-CM with 808-nm laser irradiation caused significant necrosis of tumor cells (Figure 5d). The mild PTT from Au@Rh-CM combined with laser irradiation only resulted in moderate necrotic/apoptotic cell killing. No obvious destruction could be seen in the tumors treated with either 808-nm laser irradiation or Au@Rh-ICG-CM alone.

Immunofluorescence staining was also performed on the tissue sections to evaluate the capability of Au@Rh-ICG-CM in relieving tumor hypoxia by using fluorescently tagged antibodies against endogenous hypoxia-inducible factor (HIF)-lα (green) and a platelet endothelial cell adhesion molecule (CD31, red).[50] Tumor hypoxia induced expression of HIF-1α[51] can be used as an indirect indicator of hypoxic microenvironment, while CD31 visualizes tumor vascularization.[52] In contrast to bright green fluorescence in control tumors, negligible fluorescence was detected in the tumors treated with Au@Rh-CM or Au@Rh-ICG-CM (Figure 5e), implying this nanosystem indeed alleviated the hypoxic conditions of tumor microenvironment. To further confirm the hypoxia of tumors while evaluate oxygen production in vivo, the tumor sections were also analyzed with another commercial hypoxyprobe (pimonidazole) immunofluorescence assay kit, in which the hypoxic areas were stained with fluorescently labeled antibody against pimonidazole.[53] Notably, tumors treated with Au@Rh-CM and Au@Rh-ICG-CM showed marked low fluorescence intensity (Figure S26a, Supporting Information) compared with the controls. Semiquantitative analysis of the positive hypoxic area and microvessel density clearly revealed that Au@Rh-CM and Au@Rh-ICG-CM could efficiently relieve tumor hypoxia without obvious alteration of tumor vasculature (Figure 5f and Figure S26b, Supporting Information). To determine whether replenishment of O_2 in tumors was able to elevate the ROS level, dihydroethidium (DHE) probe, which can be oxidized into ethidium by intracellular ROS and then intercalate into DNA to produce red fluorescence,[54] was used to stain frozen sections of tumors. As shown in Figure S27 (Supporting Information), strong red fluorescence was observed in tumors treated with Au@Rh-ICG-CM and 808-nm laser irradiation, confirming a high level of ROS generation. Moreover, the production of toxic $^1O_2$ in tumors was also evaluated by using SOSG. Strong green fluorescence was observed in tumors after treated with Au@Rh-ICG-CM plus 808-nm laser irradiation (Figure S28a, Supporting Information), indicating a high level of $^1O_2$ production, as high as ≈9.4 times of the controls (Figure S28a, Supporting Information). These fluorescence staining results suggest that Au@Rh-ICG-CM is able to increase tumorous O_2 level via its catalase-like decomposition of endogenous H_2O_2 and subsequent elevation of toxic ROS concentration for enhanced PDT.

To maximize the use of animals, biosafety evaluation of Au@Rh-ICG-CM was combined with the therapeutic assessment. Multiple analyses were performed to determine the systemic toxicity of Au@Rh-ICG-CM in mice. Monitoring the body weight of mice during treatment revealed comparable weight changes among different groups (Figure S29a, Supporting Information). Biochemical analyses of blood samples collected from the mice showed comparable liver and kidney functions between Au@Rh-ICG-CM treated and nontreated mice at day 8 and 16 (Figure S29b,c, Supporting Information). Routine blood analysis of Au@Rh-ICG-CM-treated mice for 16 d also confirmed the maintenance of normal range for nine blood indexes including red blood cells (RBC), white blood cell (WBC), hemoglobin (HGB), hematocrit (HCT), platelets (PLT), mean corpuscular volume (MCV), mean platelet volume (MPV), mean corpuscular hemoglobin (MCH), and mean corpuscular hemoglobin concentration (MCHC), indicating negligible blood toxicity of Au@Rh-ICG-CM (Figure S29d-l, Supporting Information). Histological analyses of major organs harvested after 16 d treatment with Au@Rh-ICG-CM showed no noticeable signs of tissue damage or inflammatory injury (Figure S29m, Supporting Information), revealing negligible toxicity of Au@Rh-ICG-CM to major organs. All of these analyses demonstrate that Au@Rh-ICG-CM nanosystems have good in vivo biocompatibility as a promising therapeutic agent for future application.

In sum, we have successfully synthesized biometallic and biphasic core–shell Au@Rh nanostructures with mesopores in the Rh shell and used them to develop a new nanotherapeutic agent, Au@Rh-ICG-CM, which can effectively modulate the hypoxic tumor microenvironment with demonstrated improvement of PDT therapeutic efficiency. The porous Au@Rh core–shell nanostructures exhibit a high efficiency to catalyze H_2O_2-to-O_2 decomposition and effectively relieve the hypoxic challenge in tumors. Meanwhile, with the assistance of homologous tumor CM, photosensitizer ICG-loaded Au@Rh nanostructures preferably accumulate in the tumor site to produce tumor toxic $^1O_2$. Moreover, the mild temperature increases in tumor sites caused by photothermal effect of Au@Rh-ICG-CM further promotes cellular uptake of ICG and consequent generation of $^1O_2$, thereby strengthening its PDT efficacy. In vitro cellular studies show that Au@Rh-ICG-CM can catalyze the decomposition of endogenous H_2O_2 into O_2 and then enhance PDT efficacy under a simulated hypoxic condition. In vivo experiments further demonstrate that Au@Rh-ICG-CM can effectively alleviate tumor hypoxia and therefore yield increased therapeutic efficiency upon laser irradiation of tumors. Overall, the reported findings provide a new route to synthesize a bimetallic Rh- based core–shell nanosystems with catalase-like capacity along with demonstration of their potential utility for cancer therapy in hypoxic tumor microenvironments via enhanced PDT. With this said, the current nanosystem may also find other possible use in treating those pathophysiological conditions with moderately elevated H_2O_2, such as in the chronic ulcers to reduce the oxidative stress due to prolonged inflammations.[55] Besides, we believe the simplicity of the synthesis method for Au@Rh can be extended to other bi- or tri-metallic nanostructures as demonstrated with Au@Pt (inset of Figure 1j) in this report to achieve enhanced catalytic ability in comparison with monometals.[56] Furthermore, it is worth mentioning that the biphasic core–shell nanocrystals, unlike many doped or alloyed nanostructures,[57] can also be used to achieve heterogeneous catalysis with the possibility of individually tailoring the core and shell with the metals for desired catalytic potential and specificity.

Experimental Section

Methods and any associated references are available in the Supporting Information.

Supplementary Material

Refer to Web version on PubMed Central for supplementary material.

Acknowledgements

This study was financially supported by National Science Foundation (NSF-DMR Award No. 1508511), NIAMS award number 1R01AR067859 and National Science Foundation of China (U190420008, 31870994). The authors would like to thank Dr. Tong Wang and Sheng Zhang from the Advanced Science Research Center at Graduate Center of CUNY for collecting the TEM images. The authors are also grateful for help from Thomas Cattabiani (Stevens Institute of Technology) for proofreading. All animal experiments were carried out in accordance with the guidelines evaluated and approved by the ethics committee of Xiamen University. MDA-MB-231 cells and HUVECs were both purchased from American Type Culture Collection (ATCC, Rockville, MD).

References

[1]. Rankin EB, Giaccia AJ, Science 2016, 352, 175. [PubMed: 27124451]

[2] a). Liu JN, Bu W, Shi J, Chem. Rev 2017, 117, 6160; [PubMed: 28426202] b)Lv W, Zhang Z, Zhang KY, Yang H, Liu S, Xu A, Guo S, Zhao Q, Huang W, Angew. Chem., Int. Ed 2016, 55, 9947;c)Shannon AM, Bouchier-Hayes DJ, Condron CM, Toomey D, Cancer Treat. Rev 2003, 29, 297; [PubMed: 12927570] d)Zhang R, Song X, Liang C, Yi X, Song G, Chao Y, Yang Y, Yang K, Feng L, Liu Z, Biomaterials 2017, 138, 13; [PubMed: 28550753] e)Huang X, Zhuang J, Chung SW, Huang B, Halpert G, Negron K, Sun X, Yang J, Oh Y, Hwang PM, Hanes J, Suk JS, ACS Nano 2019, 13, 236; [PubMed: 30576113] f)Larue L, Myrzakhmetov B, Ben-Mihoub A, Moussaron A, Thomas N, Arnoux P, Baros F, Vanderesse R, Acherar S, Frochot C, Pharmaceuticals 2019, 12, 163.

[3] a). Domans DE, Fukumura D, Jain RK, Nat. Rev. Cancer 2003, 3, 380; [PubMed: 12724736] b)Huang L, Li Z, Zhao Y, Yang J, Yang Y, Pendharkar AI, Zhang Y, Kelmar S, Chen L, Wu W, Zhao J, Han G, Adv. Mater 2017, 29, 1604789;c)Bhaumik J, Mittal AK, Banerjee A, Chisti Y, Banerjee UC, Nano Res. 2014, 8, 1373.

[4] a). Li J, Wei K, Zuo S, Xu Y, Zha Z, Ke W, Chen H, Ge Z, Adv. Funct. Mater 2017, 27, 1702108;b)Li X, Kwon N, Guo T, Liu Z, Yoon J, Angew. Chem., Int. Ed. Engl 2018, 57, 11522. [PubMed: 29808948]

[5] a). Qian C, Yu J, Chen Y, Hu Q, Xiao X, Sun W, Wang C, Feng P, Shen QD, Gu Z, Adv. Mater 2016, 28, 3313; [PubMed: 26948067] b)Manda G, Hinescu ME, Neagoe IV, Ferreira LFV, Boscencu R, Vasos P, Basaga SH, Cuadrado A, Curr. Pharm. Des 2018, 24, 5268. [PubMed: 30674246]

[6] a). Idris NM, Gnanasammandhan MK, Zhang J, Ho PC, Mahendran R, Zhang Y, Nat. Med 2012, 18, 1580; [PubMed: 22983397] b)Mallidi S, Anbil S, Bulin AL, Obaid G, Ichikawa M, Hasan T, Theranostics 2016, 6, 2458. [PubMed: 27877247]

[7] a). Jia Q, Ge J, Liu W, Zheng X, Chen S, Wen Y, Zhang H, Wang P, Adv. Mater 2018, 30, 1706090;b)Xia D, Xu P, Luo X, Zhu J, Gu H, Huo D, Hu Y, Adv. Funct. Mater 2019, 29, 1807294;c)Zhang K, Yu Z, Meng X, Zhao W, Shi Z, Yang Z, Dong H, Zhang X, Adv. Sci 2019, 6, 1900530.

[8] a). Chen Z, Niu M, Chen G, Wu Q, Tan L, Fu C, Ren X, Zhong H, Xu K, Meng X, ACS Nano 2018, 12, 12721; [PubMed: 30512923] b)Gao S, Wang G, Qin Z, Wang X, Zhao G, Ma Q, Zhu L, Biomaterials 2017 112, 324. [PubMed: 27776285]

[9] a). Wang J, Liu L, You Q, Song Y, Sun Q, Wang Y, Cheng Y, Tan F, Li N, Theranostics 2018, 8, 955; [PubMed: 29463993] b)Cheng Y, Cheng H, Jiang C, Qiu X, Wang K, Huan W, Yuan A, Wu J, Hu Y, Nat. Commun 2015, 6, 8785. [PubMed: 26525216]

[10] a). Zheng DW, Li B, Li CX, Fan JX, Lei Q, Li C, Xu Z, Zhang XZ, ACS Nano 2016, 10, 8715; [PubMed: 27532320] b)Huang CC, Chia WT, Chung MF, Lin KJ, Hsiao CW, Jin C, Lim WH, Chen CC, Sung GW, J. Am. Chem. Soc 2016, 138, 5222; [PubMed: 27075956] c)Liu LH, Zhang YH, Qiu WX, Zhang L, Gao F, Li B, Xu L, Fan JX, Li ZH, Zhang XZ, Small 2017, 13, 1701621.

[11] a). Huang X, Deng G, Han Y, Yang G, Zou R, Zhang Z, Sun S, Hu J, Adv. Sci 2019, 6, 1901461;b)Yao C, Wang W, Wang P, Zhao M, Li X, Zhang F, Adv. Mater 2018, 30, 1704833;c)Yang Y, Chen M, Wang B, Wang P, Liu Y, Zhao Y, Li K, Song G, Zhang XB, Tan W, Angew. Chem., Int. Ed 2019, 58, 15069;d)Liu J, Liu T, Du P, Zhang L, Lei J, Angew. Chem., Int. Ed 2019, 131, 7890.

[12] a). Wang D, Wu H, Lim WQ, Phua SZF, Xu P, Chen Q, Guo Z, Zhao Y, Adv. Mater 2019, 31, 1901893;b)Lambeth JD, Nat. Rev. Immunol 2004, 4, 181; [PubMed: 15039755] c)Szatrowski TP, Nathan CF, Cancer Res. 1991, 51, 794. [PubMed: 1846317]

[13]. Wang J, Zhang B, Sun J, Wang Y, Wang H, Adv. Ther 2019, 1900083.

[14] a). Chen Q, Feng L, Liu J, Zhu W, Dong Z, Wu Y, Liu Z, Adv. Mater 2016, 28, 7129; [PubMed: 27283434] b)Kim J, Kim HY, Song SY, Go S, Sohn HS, Baik S, Soh M, Kim K, Kim D, Kim H-C, Lee N, Kim B-S, Hyeon T, ACS Nano 2019, 13, 3206; [PubMed: 30830763] c)Wang X, Zeng J, Zhang M, Zeng X, Zhang X, Adv. Funct. Mater 2018, 28, 1801783;d)Wei J, Li J, Sun D, Li Q, Ma J, Chen X, Zhu X, Zheng N, Adv. Funct. Mater 2018, 28, 1706310.

[15]. Chen H, Tian J, He W, Guo Z, J. Am. Chem. Soc 2015, 137, 1539. [PubMed: 25574812]

[16]. Prasad P, Gordijo CR, Abbasi AZ, Maeda A, Ip A, Rauth AM, DaCosta RS, Wu XY, ACS Nano 2014, 8, 3202. [PubMed: 24702320]

[17]. Kim J, Cho HR, Jeon H, Kim D, Song C, Lee N, Choi SH, Hyeon T, J. Am. Chem. Soc 2017, 139, 10992. [PubMed: 28737393]

[18]. Kang S, Shin W, Choi MH, Ahn M, Kim YK, Kim S, Min DH, Jang H, ACS Nano 2018, 12, 6997. [PubMed: 29901981]

[19]. Mckee DW, J. Catal 1969, 14, 355.

[20]. García S, Zhang L, Piburn GW, Henkelman G, Humphrey SM, ACS Nano 2014, 8, 11512. [PubMed: 25347078]

[21]. Wang S, Huang P, Nie L, Xing R, Liu D, Wang Z, Lin J, Chen S, Niu F, Lu G, Chen X, Adv. Mater 2013, 25, 3055. [PubMed: 23404693]

[22]. Song G, Liang C, Yi X, Zhao Q, Cheng L, Yang K, Liu Z, Adv. Mater 2016, 28, 2716. [PubMed: 26848553]

[23]. Tao F, Grass ME, Zhang Y, Butcher DR, Renzas JR, Liu Z, Chung JY, Mun BS, Salmeron M, Somorjai GA, Science 2008, 322, 932. [PubMed: 18845713]

[24]. Kang J, Joo J, Kwon EJ, Skalak M, Hussain S, She ZG, Ruoslahti E, Bhatia SN, Sailor MJ, Adv. Mater 2016, 28, 7962. [PubMed: 27383373]

[25]. Zhou J, Jiang Y, Hou S, Upputuri PK, Wu D, Li J, Wang P, Zhen X, Pramanik M, Pu K, Duan H, ACS Nano 2018, 12, 2643. [PubMed: 29438610]

[26] a). Mittendorfer F, Seriani N, Dubay O, Kresse G, Phys. Rev. B 2007, 76, 233413;b)Yu NF, Tian N, Zhou ZY, Huang L, Xiao J, Wen YH, Sun SG, Angew. Chem., Int. Ed 2014, 53, 5097.c)Li C, Tan H, Lin J, Luo X, Wang S, You J, Kang Y-M, Bando Y, Yamauchi Y, Kim J, Nano Today 2018, 21, 91;d)Li C, Iqbal M, Jiang A, Wang Z, Kim J, Nanjundan AK, Whitten AE, Wood K, Yamauchi Y, Chem. Sci 2019, 10, 4054; [PubMed: 31015946] e)Ataee-Esfahani H, Nemoto Y, Wang L, Yamauchi Y, Chem. Commun 2011, 47, 3885.

[27]. Hoefelmeyer JD, Niesz K, Somorjai GA, Tilley TD, Nano Lett. 2005, 5, 435. [PubMed: 15755090]

[28] a). Jiang B, Li C, Dag O, Abe H, Takei T, Imai T, Hossain MSA, Islam MT, Wood K, Henzie J, Yamauchi Y, Nat. Commun 2017, 8, 15581; [PubMed: 28524873] b)Li C, Iqbal M, Lin J, Luo X, Jiang B, Malgras V, Wu KC, Kim J, Yamauchi Y, Acc. Chem. Res 2018, 51, 1764. [PubMed: 29984987]

[29]. Lin LS, Yang X, Zhou Z, Yang Z, Jacobson O, Liu Y, Yang A, Niu G, Song J, Yang HH, Chen X, Adv. Mater 2017, 29, 1606681.

[30] a). Cheng YJ, Luo GF, Zhu JY, Xu XD, Zeng X, Cheng DB, Li YM, Wu Y, Zhang XZ, Zhuo RX, He F, ACS Appl. Mater. Interfaces 2015, 7, 9078; [PubMed: 25893819] b)Gu T, Cheng L, Gong F, Xu J, Li X, Han G, Liu Z, ACS Appl. Mater. Interfaces 2018, 10, 15494; [PubMed: 29682957] c)Yang ZL, Tian W, Wang Q, Zhao Y, Zhang YL, Tian Y, Tang YX, Wang SJ, Liu Y, Ni QQ, Lu GM, Teng ZG, Zhang LJ, Adv. Sci 2018, 5, 1700847.

[31]. Balasubramanian V, Correia A, Zhang H, Fontana F, Makila E, Salonen J, Hirvonen J, Santos HA, Adv. Mater 2017, 29, 1605375.

[32]. Fang RH, Kroll AV, Gao W, Zhang L, Adv. Mater 2018, 30, 1706759.

[33]. Sun H, Su J, Meng Q, Yin Q, Chen L, Gu W, Zhang Z, Yu H, Zhang P, Wang S, Li Y, Adv. Mater 2016, 28, 9581. [PubMed: 27628433]

[34]. Wan G, Chen B, Li L, Wang D, Shi S, Zhang T, Wang Y, Zhang L, Wang Y, Biomaterials 2018, 155, 25. [PubMed: 29161627]

[35]. You Q, Sun Q, Wang J, Tan X, Pang X, Liu L, Yu M, Tan F, Li N, Nanoscale 2017, 9, 3784; [PubMed: 28067380] Feng B, Niu Z, Hou B, Zhou L, Li Y, Yu H, Adv. Funct. Mater 2019, 1906605.

[36]. Cheng L, Zhang F, Wang S, Pan X, Han S, Liu S, Ma J, Wang H, Shen G, Liu H, Yuan Q, Angew. Chem., Int. Ed 2019, 58, 7728.

[37]. Repasky EA, Evans SS, Dewhirst MW, Cancer Immunol. Res 2013, 1, 210. [PubMed: 24490177]

[38]. Tao FF, Chem. Soc. Rev 2012, 41, 7977. [PubMed: 23143202]

[39]. Liang S, Deng X, Chang Y, Sun C, Shao S, Xie Z, Xiao X, Ma P, Zhang H, Cheng Z, Lin J, Nano Lett. 2019, 19, 4134. [PubMed: 31084016]

[40] a). Góth L, Clin. Chim. Acta 1991, 196, 143; [PubMed: 2029780] b)Feng L, Dong Z, Liang A, Chen M, Tao D, Cheng L, Yang K, Liu Z, Biomaterials 2018, 181, 81. [PubMed: 30077139]

[41]. Ge C, Wu R, Chong Y, Fang G, Jiang X, Pan Y, Chen C, Yin JJ, Adv. Funct. Mater 2018, 28, 1801484.

[42]. Zhai S, Hu X, Hu Y, Wu B, Xing D, Biomaterials 2017, 121, 41. [PubMed: 28068593]

[43]. Li T, Zhou J, Wang L, Zhang H, Song C, de la Fuente JM, Pan Y, Song J, Zhang C, Cui D, Adv. Healthcare Mater 2019, 8, 1900192.

[44]. Villa C, Campione M, Santiago-González B, Alessandrini F, Erratico S, Zucca I, Bruzzone MG, Forzenigo L, Malatesta P, Mauri M, Trombetta E, Brovelli S, Torrente Y, Meinardi F, Monguzzi A, Adv. Funct. Mater 2018, 28, 1707582.

[45]. Zamojc K, Zdrowowicz M, Rudnicki-Velasquez PB, Krzyminski K, Zaborowski A, Niedzialkowski P, Jacewicz D, Chmurzynski L, Free Radical Res. 2017, 51, 38. [PubMed: 27866421]

[46] a). Ragas X, Jimenez-Banzo A, Sanchez-Garcia D, Batllori X, Nonell S, Chem. Commun 2009, 20, 2920;b)Vankayala R, Sagadevan A, Vijayaraghavan P, Kuo CL, Hwang KC, Angew. Chem., Int. Ed. Engl 2011, 50, 10640. [PubMed: 21932210]

[47]. Chen Z, Zhao P, Luo Z, Zheng M, Tian H, Gong P, Gao G, Pan H, Liu L, Ma A, Cui H, Ma Y, Cai L, ACS Nano 2016, 10, 10049. [PubMed: 27934074]

[48]. Liu Y,Bhattarai P,Dai Z, Chen X, Chem. Soc. Rev 2019,48, 2053. [PubMed: 30259015]

[49]. Yi X, Yang K, Liang C, Zhong X,Ning P, Song G, Wang D, Ge A, Chen C, Chai Z, Liu Z, Adv. Funct. Mater 2015, 25, 4689.

[50]. Phua SZF, Yang G, Lim WQ, Verma A, Chen H, Thanabalu T, Zhao Y, ACS Nano 2019, 13, 4742. [PubMed: 30964974]

[51]. Xu S, Zhu X, Zhang C, Huang W, Zhou Y, Yan D, Nat. Commun 2018, 9, 2053. [PubMed: 29795534]

[52]. Mei KC, Bai J, Lorrio S, Wang JT, Al-Jamal KT, Biomaterials 2016, 106, 276. [PubMed: 27573135]

[53] a). Zheng X, Mao H, Huo D, Wu W, Liu B, Jiang X, Nat. Biomed. Eng 2017, 1, 0057;b)Kaanders JHAM, Wijffels KIEM, Marres HAM, Ljungkvist ASE, Pop LAM, van den Hoogen FJA, de Wilde PCM, Bussink J, Raleigh JA, van der Kogel AJ, Cancer Res. 2002, 62, 7066. [PubMed: 12460928]

[54]. Han Y, Chen Z, Zhao H, Zha Z, Ke W, Wang Y, Ge Z, J. Controlled Release 2018, 284, 15.

[55]. Wlaschek M, Kochanek KS, Wound Repair Regener. 2005, 13, 452.

[56]. Kang SW, Lee YW, Park Y, Choi BS, Hong JW, Park KH, Han SW, ACS Nano 2013, 7, 7945. [PubMed: 23915173]

[57]. Henning AM, Watt J, Miedziak PJ, Cheong S, Santonastaso M, Song M, Takeda Y, Kirkland AI, Taylor SH, Tilley RD, Angew. Chem., Int. Ed 2013, 52, 1477.

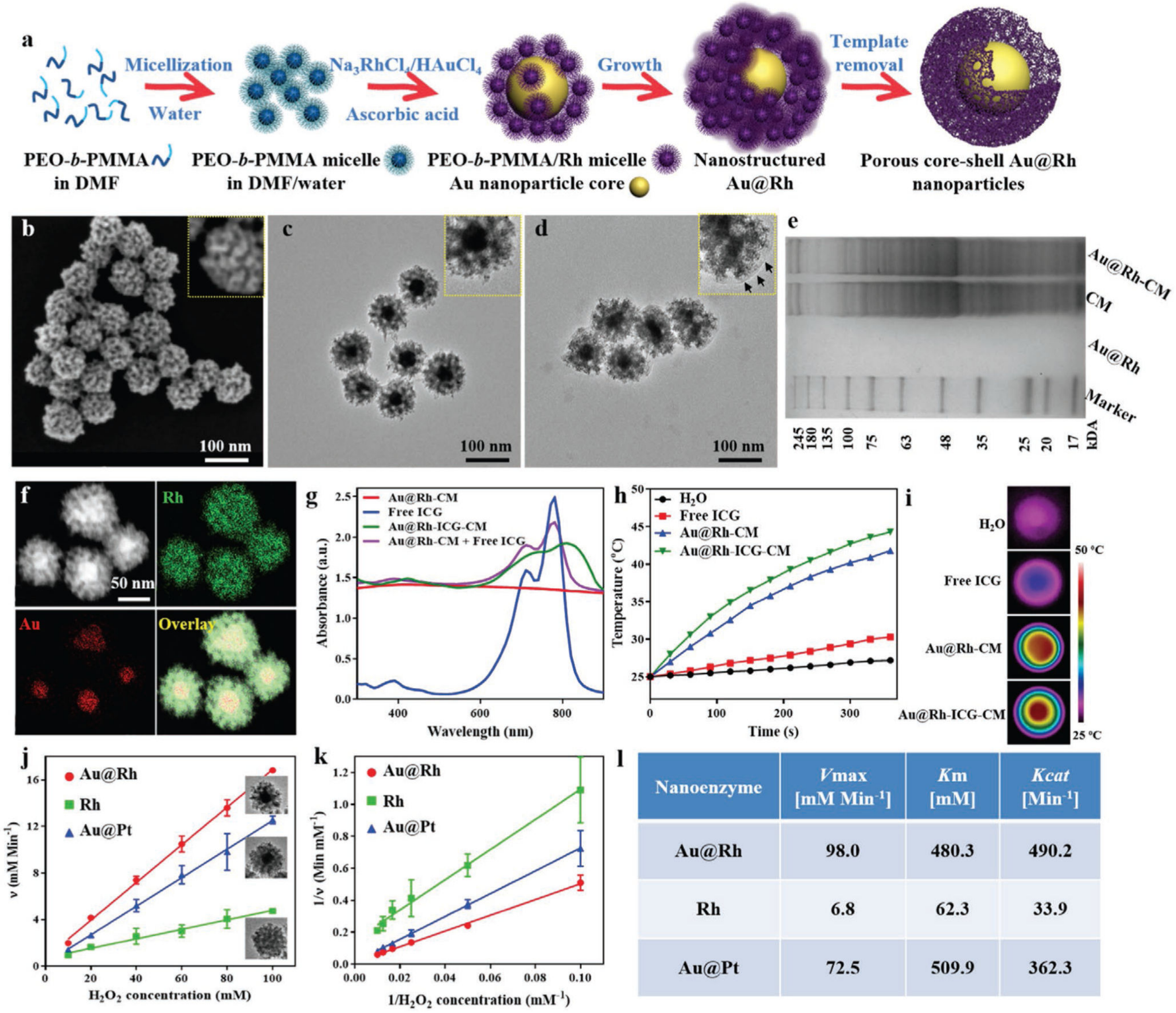

Nanoenzyme	*V*max [mM Min^{-1}]	*K*m [mM]	*Kcat* [Min^{-1}]
Au@Rh	98.0	480.3	490.2
Rh	6.8	62.3	33.9
Au@Pt	72.5	509.9	362.3

Figure 1.

a) Schematic illustration of the processes in formation of porous Au@Rh core–shell nanostructures. b) Representative SEM image of the surfaces of as-prepared Au@Rh nanostructures to show the presence of mesopores. c) Representative TEM images of Au@Rh nanostructures to confirm the existence of a dense core and porous shell in individual nanostructures. d) Representative TEM images of Au@Rh-CM nanostructures to confirm the presence of cell membrane on the nanostructure surface. Au@Rh-CM nanostructures were stained with uranyl acetate to increase the contrast of cell membrane (arrows in inset). e) SDS-PAGE protein analysis of Au@Rh, CM, and Au@Rh-CM. f) STEM-HAADF image and corresponding EDS elemental mapping of Au and Rh of Au@Rh nanostructures. g) UV–vis–NIR absorption spectra of Au@Rh-CM, free ICG, Au@Rh-ICG-CM, and the physically mixed Au@Rh-CM and free ICG. h) Heating curves of free ICG, Au@Rh-CM, and Au@Rh-ICG-CM compared to DI water only under 808-nm laser irradiation (0.3 W cm^{-2}). i) Photothermal images of DI water, free ICG, Au@Rh-CM, and

Au@Rh-ICG-CM under 808-nm laser irradiation (0.3 W cm^{-2}, 360 s). j) The velocity of the catalytic reaction was measured using different nanostructures and different concentrations of H_2O_2. Inset is TEM image of the corresponding nanostructures. Data are expressed as mean ± SD ($n = 3$). k) Double-reciprocal plots to determine the kinetic constants of three types of nanostructures for H_2O_2 substrate. Data are expressed as mean ± SD ($n = 3$). l) Comparison of the kinetic parameters of various nanostructures toward H_2O_2.

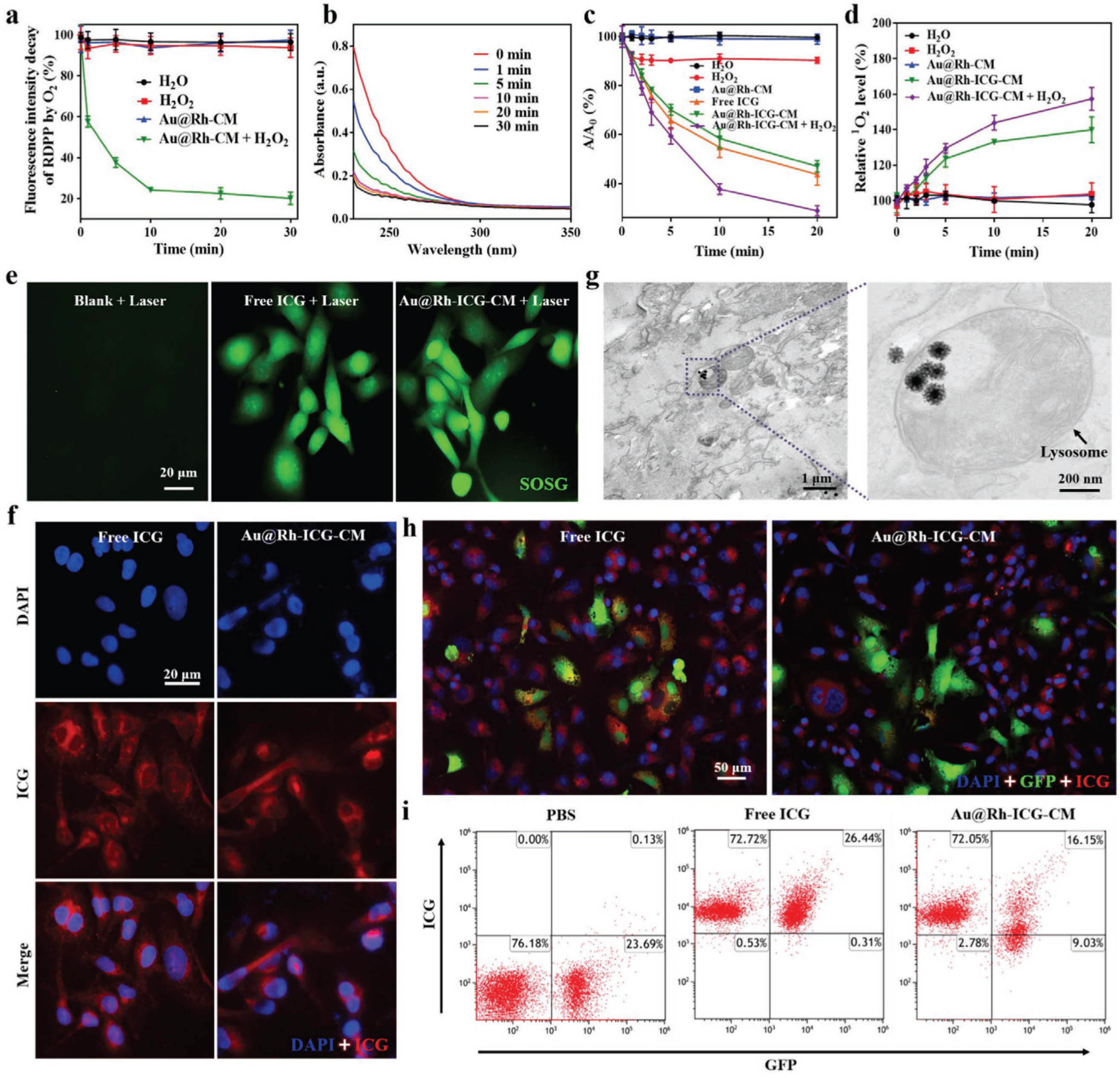

Figure 2.

a) Generation of O_2 from H_2O_2 aqueous solution (1×10^{-4} m) with the catalysis of Au@Rh-CM (50 µg mL^{-1}). Data are expressed as mean ± SD (*n* = 3). b) UV–vis spectra of H_2O_2 remained in the reaction with Au@Rh-CM at different time points (*n* = 3, independent experiments). c) ROS-induced absorbance changes of DPBF at 410 nm after irradiation (808 nm, 0.3 W cm^{-2}) for different times in water, H_2O_2, free ICG, Au@Rh-CM, Au@Rh-ICG-CM, or Au@Rh-ICG-CM + H_2O_2 solution. A_0 is the initial absorbance of DPBF probe. Data are expressed as mean ± SD (*n* = 3). d) Elevated generation of singlet oxygen upon laser irradiation (808 nm, 0.3 W cm^{-2}) for different times in water, H_2O_2, Au@Rh-CM, or Au@Rh-ICG-CM solution with or without H_2O_2. Singlet oxygen was detected by the fluorescence probe of SOSG. Data are expressed as mean ± SD (*n* = 3). e) MDA-MB-231 cells treated with free ICG or Au@Rh-ICG-CM nanocomposites under laser irradiation (808 nm, 0.3 W cm^{-2}, 3 min). Green fluorescence represents intracellular singlet oxygen production. Experiments were performed for three times independently. f) Fluorescence images of MDA-MB-231 cells incubated with free ICG or Au@Rh-ICG-CM for 6 h (*n* = 3, independent experiments). g) TEM image of MDA-MB-231 cells incubated with Au@Rh-ICG-CM for 6 h, showing the intracellular localization in lysosomes (arrow). Each bio-TEM observation was performed on three cell sections collected from respective culture dishes, and the representative images are presented. h) Fluorescence images of the coculture of MDA-MB-231 cells and GFP-labeled HUVECs after respective incubation with free ICG and Au@Rh-ICG-CM (*n* = 3, independent experiments). i) Flow cytometry analyses of the cocultured MDA-MB-231 and GFP-labeled HUVEC cells after incubation with PBS, free ICG, and Au@Rh-ICG-CM, respectively. Experiments were repeated three times independently.

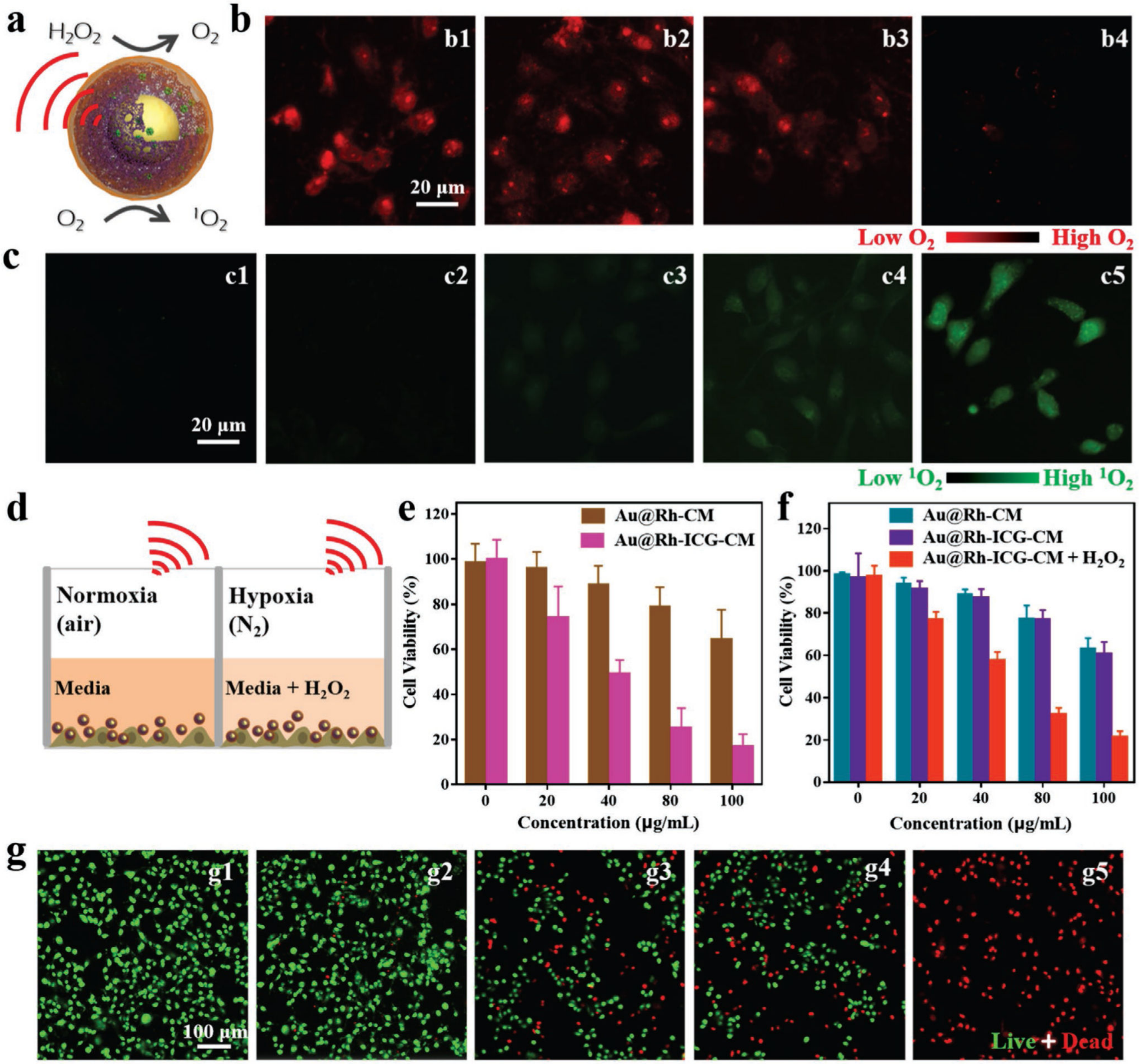

Figure 3.

a) Schematic illustration of O_2 generation and $^1O_2$ production catalyzed by Au@Rh-CM. b) Fluorescence images of O_2 generation in MDA-MB-231 cells in a hypoxic setting (i.e., N_2 atmosphere) treated with: b1) no treatment, b2) H_2O_2, b3) Au@Rh-CM, and b4) Au@Rh-CM + H_2O_2. Experiments were repeated three times independently. c) Fluorescence images of singlet oxygen production in MDA-MB-231 cells in N_2 atmosphere treated with: c1) no treatment, c2) Au@Rh-ICG-CM in dark, c3) Au@Rh-CM under 808-nm laser irradiation, c4) Au@Rh-ICG-CM under 808-nm laser irradiation, and c5) Au@Rh-ICG-CM + H_2O_2 under 808-nm laser irradiation. Irradiation time was 3 min. Experiments were performed three times independently. d) Schematic illustration of MDA-MB-231 cells treated with Au@Rh-ICG-CM and laser irradiation in normoxia (air atmosphere) and hypoxia (N_2

atmosphere). e) Viability of MDA-MB-231 cells treated with Au@Rh-CM or Au@Rh-ICG-CM plus 808-nm laser irradiation (3 min) under normoxia (air atmosphere). Data are expressed as mean ± SD (*n* = 6). f) Viability of MDA-MB-231 cells treated with Au@Rh-CM, Au@Rh-ICG-CM, or Au@Rh-ICG-CM/H_2O_2 plus 808-nm laser irradiation (3 min) under hypoxia (N_2 atmosphere). Data are expressed as mean ± SD (*n* = 6). g) Fluorescence images of hypoxic MDA-MB-231 cells after different treatments: g1) no treatment in dark, g2) Au@Rh-ICG-CM in dark, g3) Au@Rh-CM under 808-nm laser irradiation, g4) Au@Rh-ICG-CM under 808-nm laser irradiation, and g5) Au@Rh-ICG-CM/H_2O_2 under 808 nm laser irradiation. Cells were stained live (green) with calcein (AM) and dead (red) with propidium iodide (PI). The irradiation time was 3 min. Experiments were repeated three times independently.

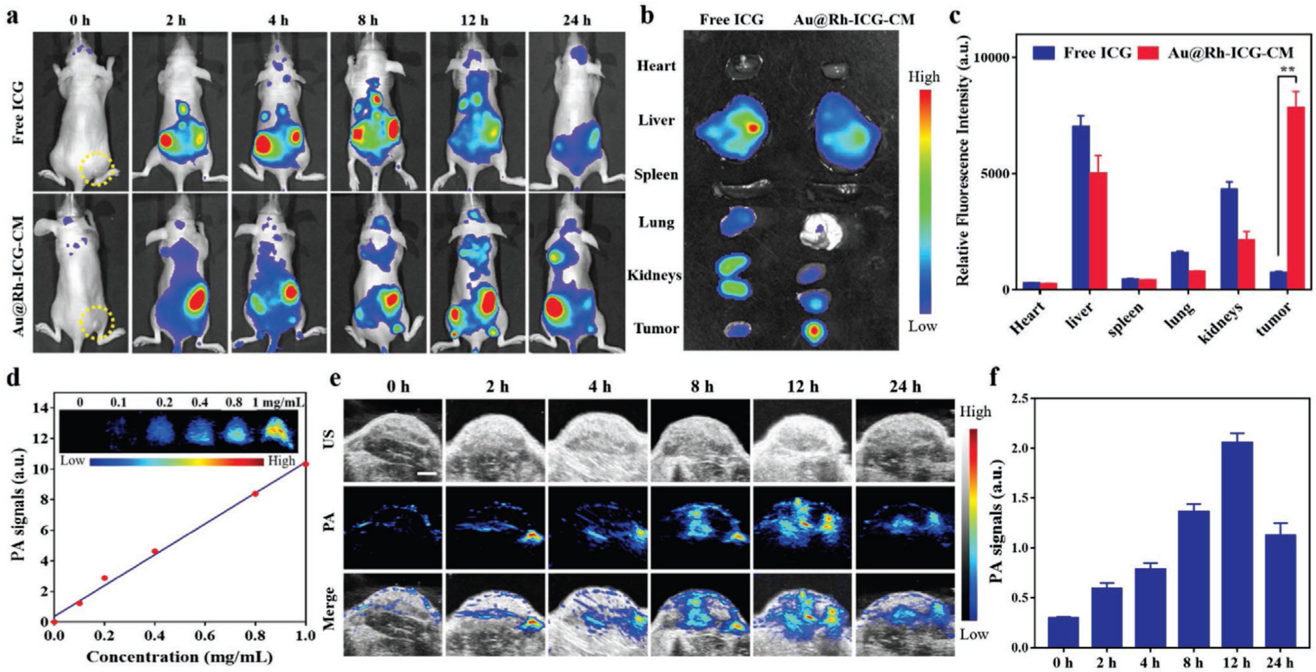

Figure 4.

a) Representative in vivo fluorescence images of MDA-MB-231-tumor-bearing mice at indicated time points (0, 2, 4, 8, 12, and 24 h) after intravenous injection of free ICG and Au@Rh-ICG-CM ($n = 3$). b) Ex vivo images of excised organs and tumors examined at 24 h postinjection ($n = 3$). c) Semiquantitative analyses of fluorescence intensity from these organs and tumors. Data are expressed as mean ± SD ($n = 3$). Statistical significance was assessed by unpaired Student's t-test. $^{**}p < 0.01$. d) Correlation of photoacoustic intensity with the concentration of Au@Rh-ICG-CM aqueous solutions ($n = 3$). Top: the corresponding PA images. e) Representative PA images of Au@Rh-ICG-CM at the tumor site at designated time points (0, 2, 4, 8, 12, and 24 h). f) Quantification of the time-dependent PA intensity at the tumor site in (e). Data are expressed as mean ± SD ($n = 3$).

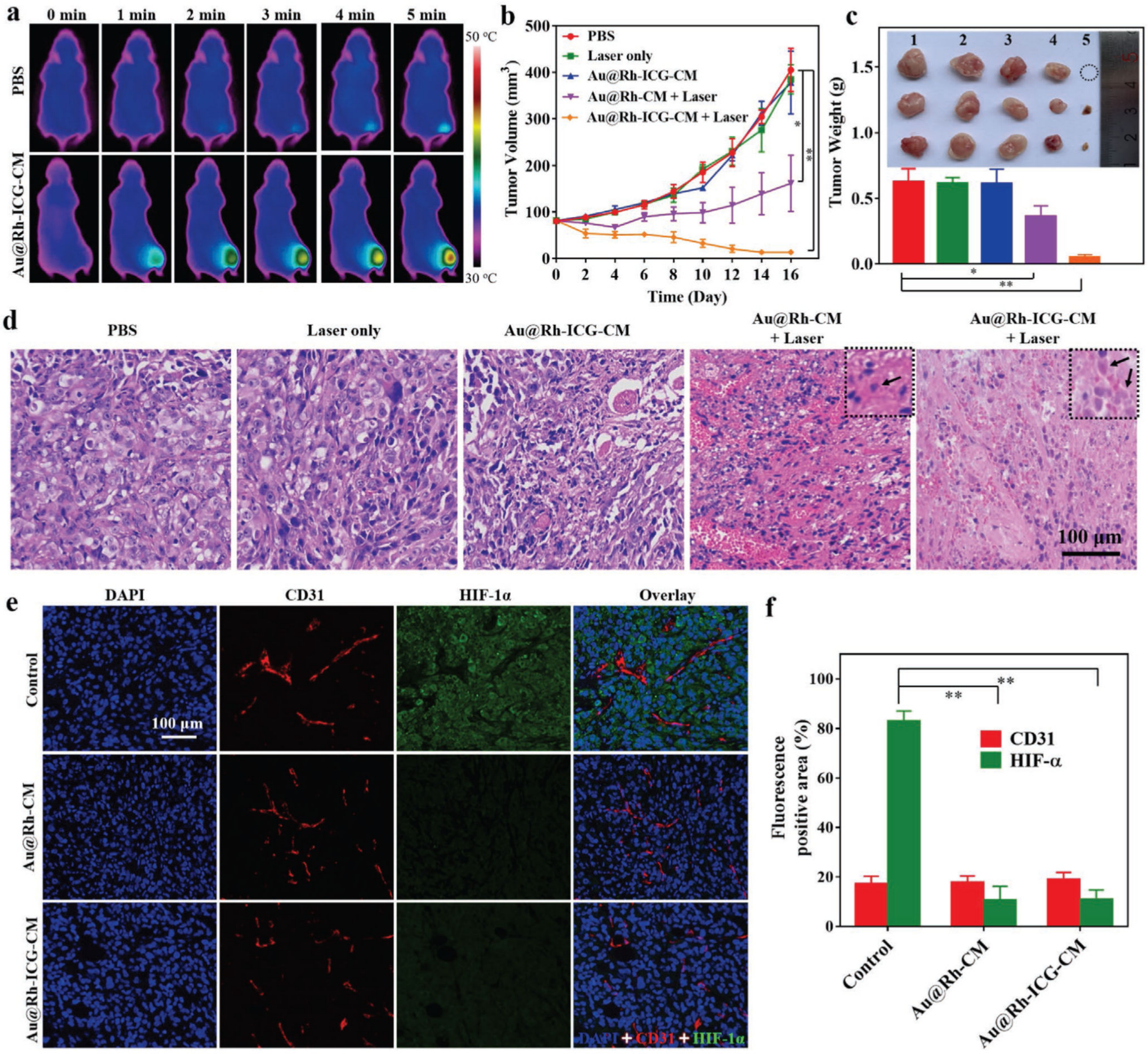

Figure 5.

a) Representative time-dependent photothermal images of MDA-MB-231-tumor-bearing mice ($n = 3$) exposed to an 808 nm laser (0.3 W cm^{-2}) for up to 5 min after intravenous injection with PBS and Au@Rh-ICG-CM (5 mg kg^{-1}), respectively. The images were recorded with an infrared camera. b) The time-dependent size changes of MDA-MB-231 tumors in nude mice after various treatments. The volume was measured using a vernier caliper. Data are expressed as mean ± SD ($n = 5$). Statistical significance was assessed by unpaired Student's t-test. *$p < 0.05$, **$p < 0.01$. c) Average weight of tumors and photos of tumors harvested from different treatment groups at the end of experiments (day 16). Group 1: PBS, Group 2: Laser only, Group 3: Au@Rh-ICG-CM, Group 4: Au@Rh-CM + Laser, and Group 5: Au@Rh-ICG-CM + Laser. Data are expressed as mean ± SD ($n = 5$). Statistical significance was assessed by unpaired Student's t-test. *$p < 0.05$, **$p < 0.01$. d)

Representative microscopy images of tumor cross sections stained with hematoxylin and eosin (H&E) from different treatment groups after 16 d ($n = 5$). Arrows indicate necrotic cells. e) Representative fluorescence images of tumor sections from mice treated with PBS (control), Au@Rh-CM, or Au@Rh-ICG-CM ($n = 3$). Thin tissue sections were immunofluorescently stained for microvessels (CD31, red), hypoxia (HIF-1α, green), and cell nuclei (DAPI, blue). f) Quantification of tumor hypoxia and blood vessels for different groups shown in (e). The relative hypoxia positive areas and blood vessel densities as recorded from more than five images for each group were analyzed by ImageJ (NIH). Data are shown as mean ± SD. Statistical significance was assessed by unpaired Student's t-test. $^{**}p < 0.01$.

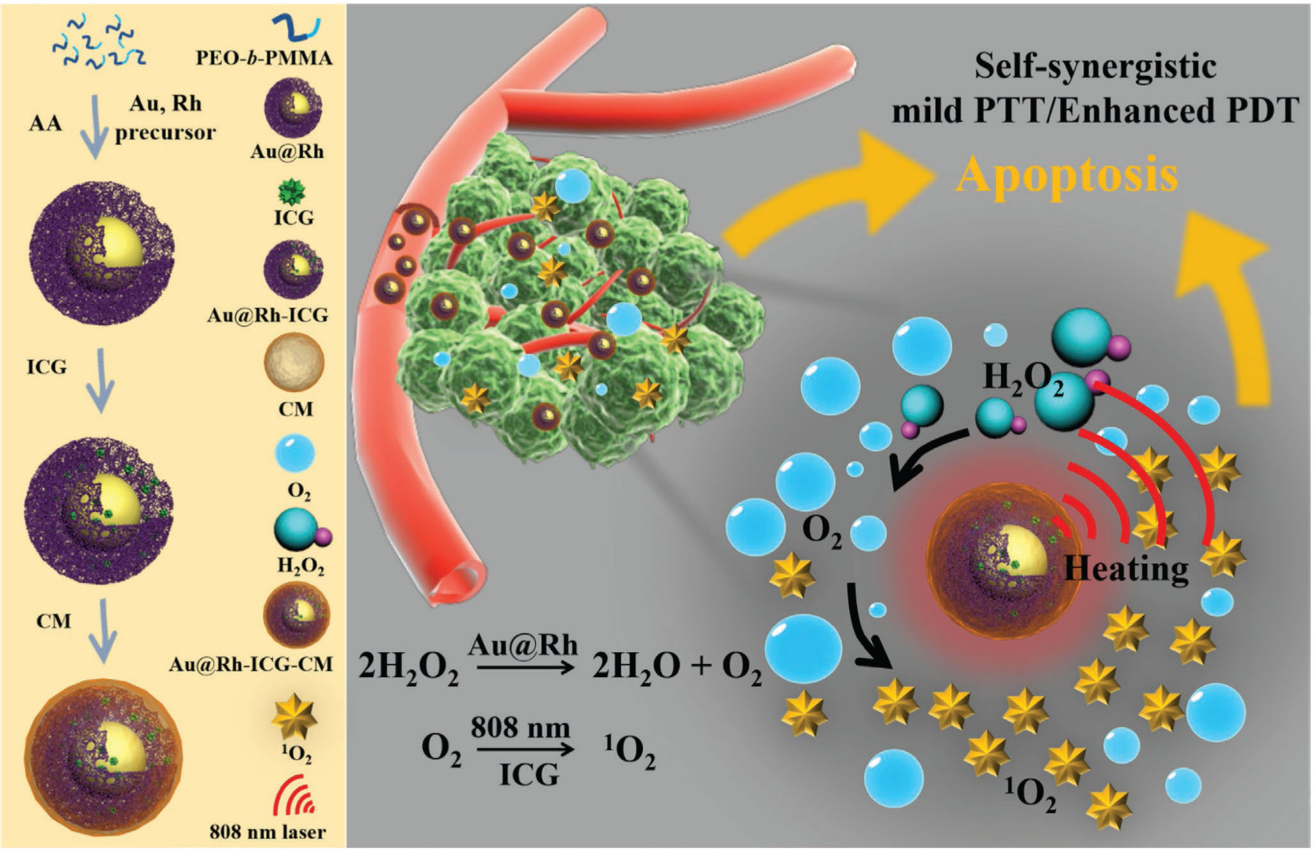

Scheme 1.

Schematic illustration to show the key steps involved in preparation of porous Au@Rh-ICG-CM core–shell nanostructures and their associated major mechanistic pathways in cancer therapy.